

Emergence of Meron Kekulé lattices in twisted Néel antiferromagnets

Kyoung-Min Kim*

Center for Theoretical Physics of Complex Systems,
Institute for Basic Science, Daejeon 34126, Republic of Korea

Se Kwon Kim†

Department of Physics, Korea Advanced Institute of Science and Technology, Daejeon 34141, Republic of Korea

A Kekulé lattice is an exotic, distorted lattice structure distinguished by alternating bond lengths in contrast to naturally formed atomic crystals. While this structure has been explored through atomic crystals and metamaterials, the possibility of forming a Kekulé lattice from topological solitons in magnetic systems has remained elusive. Here, we propose twisted bilayer easy-plane Néel antiferromagnets as a promising platform for achieving a “Meron Kekulé lattice”—a distorted topological soliton lattice comprised of antiferromagnetic merons as its lattice elements. Using atomistic spin simulations on these magnets, we demonstrate that due to the moiré-induced intricate pattern of interlayer exchange coupling, the cores of these merons are stabilized into the Kekulé-O pattern with different intracell and intercell bond lengths across moiré supercells, hence forming a Meron Kekulé lattice. Furthermore, we showcase that the two bond lengths of the Meron Kekulé lattice can be fine-tuned by adjusting the twist angle and specifics of the interlayer exchange coupling, suggesting extensive control over the meron lattice configuration in contrast to conventional magnetic systems. These discoveries pave the way for exploring topological solitons with distinctive Kekulé attributes, offering intriguing opportunities at the intersection of topological solitons and Kekulé physics.

Keywords: Kekulé lattice, topological solitons, twisted van der Waals magnets, Néel antiferromagnets, merons, twist engineering

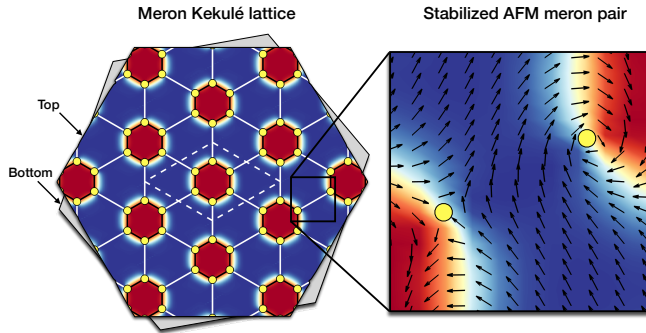


FIG. 1. Schematic illustration of a Meron Kekulé lattice in a twisted bilayer Néel antiferromagnet. Yellow dots denote the cores of antiferromagnetic (AFM) merons that form a Kekulé lattice structure. Black solid lines denote intracell bonds between meron cores within the same moiré supercell, while white solid lines denote intercell bonds between meron cores across different supercells. The white dashed line depicts a single moiré supercell. Blue color indicates parallel alignment, while red indicates antiparallel alignment between Néel vectors across the top and bottom layers. In the magnified image, arrows represent the in-plane components of Néel vectors, depicting the winding texture of a meron pair.

Merons are particle-like localized spin configurations typically found in easy-plane magnets, which exhibit both out-of-plane polarization in their core regions and

in-plane swirling textures away from the cores^{1–14}. These unique characteristics endow merons with distinctive half-integer skyrmion numbers, classifying them as topological solitons^{11,12}. The topological stability implied by the skyrmion numbers suggests merons as promising candidates for topological magnetic bits in spintronics, capable of storing and transmitting information^{15–19}. However, in continuous magnetic systems, merons typically exist alongside their counterparts, namely antimerons, and often exhibit instability against pair annihilation^{6,7,14}. Consequently, merons may manifest in limited forms such as transient states^{6,7,14}, aggregated groups^{5,8–10}, or a square lattice form as observed in chiral magnet $\text{Co}_8\text{Zn}_9\text{Mn}_3$ ¹¹. The potential instabilities and constrained manifestations of merons hinder the comprehensive study of their fundamental properties and the exploration for future technological applications.

A Kekulé lattice is a distorted lattice structure distinguished by alternating bond lengths. This lattice distortion, often referred to as Kekulé distortion, has been suggested to give rise to a range of intriguing physical phenomena not observed in pristine, undistorted lattices^{20–44}. Notable examples include charge fractionalization^{20,21}, chiral-symmetry breaking^{22–28}, and emergence of flat bands³¹ in engineered graphene. Additionally, the appearance of topological band structures has been demonstrated in photonic^{40,41} and phononic crystals^{42,43}. Experimentally, the Kekulé lattice has been realized in atomic crystals such as graphene through the addition of adatoms^{28,44} and intercalation³⁰. However, despite the predominant focus on such atomic crystals and metama-

* kmkim@ibs.re.kr

† sekwonkim@kaist.ac.kr

materials, the concept of a Kekulé lattice can extend beyond these systems, holding promise for broader applications across various physical systems with distinct lattice elements. Particularly fascinating is the potential creation of a Kekulé lattice from topological solitons in magnetic systems, which would introduce a novel perspective, contrasting with the traditionally observed Bravais lattice forms of topological solitons, such as the triangular lattice seen in the Abrikosov vortex lattice in superconductors⁴⁵ and the skyrmion lattice in magnetic systems⁴⁶. This intriguing possibility has remained unexplored, representing a pivotal piece yet to be uncovered within the realms of Kekulé physics.

In this study, we discover the creation of a Kekulé lattice from antiferromagnetic merons in twisted bilayer easy-plane Néel antiferromagnets. By conducting atomistic spin simulations on these magnets, we demonstrate that the cores of the antiferromagnetic merons are stabilized due to the moiré-induced spatial modulation of interlayer exchange coupling⁴⁷. Notably, the cores of these merons form a honeycomb-lattice-like structure across moiré supercells, exhibiting different intracell and intercell bond lengths (Figure 1). This distorted structure deviates from commonly observed, elementary Bravais-lattice forms^{11,46,48–50}, yet aligning with the known characteristics of the Kekulé-O pattern²⁸. Hence, we term our distorted meron lattice a “Meron Kekulé lattice.” We illustrate that the two bond lengths of the Meron Kekulé lattice can be fine-tuned by manipulating the twist angle and specifics of interlayer exchange coupling, offering a high degree of control over the stable meron lattice configuration. These discoveries present a Meron Kekulé lattice as a new classification within Kekulé lattices, introducing a novel pathway to attain this structure in atomic crystals. Moreover, the stability and adjustability of this distorted structure present intriguing possibilities for exploring topological solitons with precise control—a capability rarely achievable within conventional magnetic systems^{1–14,46,48–50}.

Results

AFM domain array. We construct twisted bilayer Néel antiferromagnets by rotating two magnetic layers in a honeycomb lattice with a relative twist angle (Figure 2a). These twisted magnets can be described using a Heisenberg spin model given by

$$H = J \sum_{l=t,b} \sum_{\langle i,j \rangle} \mathbf{S}_i^l \cdot \mathbf{S}_j^l + A \sum_{l=t,b} \sum_i (\mathbf{S}_i^l \cdot \hat{\mathbf{z}})^2 + \sum_{i,j} J_{ij}^\perp \mathbf{S}_i^t \cdot \mathbf{S}_j^b. \quad (1)$$

Here, \mathbf{S}_i^l represents the spin at site i on the top layer ($l = t$) and the bottom layer ($l = b$). The parameter $J = 1.0$ meV represents the intralayer AFM exchange interactions between nearest-neighbor spins. $A = 0.2$ meV represents the single-ion anisotropy energy favoring

in-plane spin orientations. J_{ij}^\perp represents the interlayer AFM exchange interactions that modulate as a function of the coordinate displacements $\mathbf{r}_{ij}^{tb} = \mathbf{r}_i^t - \mathbf{r}_j^b$ between two spins at i - and j - sites on the top and bottom layers, respectively. To describe the decaying behavior of J_{ij}^\perp as a function of $|\mathbf{r}_{ij}^{tb}|$, we employ the following exponential function^{51–55}:

$$J_{ij}^\perp = J_0^\perp \exp \left[-\alpha \left(|\mathbf{r}_{ij}^{tb}|/d - 1 \right) \right]. \quad (2)$$

Here, the parameter J_0^\perp represents the maximum value of J_{ij}^\perp at $|\mathbf{r}_{ij}^{tb}| = d$, where d denotes the perpendicular interlayer distance; the parameter α describes the decay rate of J_{ij}^\perp with respect to the increase of $|\mathbf{r}_{ij}^{tb}|$. We choose $\alpha = 15$ with the consideration that J_{ij}^\perp decreases to approximately 10% of J_0^\perp at the second-nearest neighbor distance between the top and bottom layers in the AA stacking (i.e., $|\mathbf{r}_{ij}^{tb}| = \sqrt{d^2 + a^2}$), where a is the nearest-neighbor distance in a honeycomb lattice. In principle, one can calculate the value of α through ab initio calculations⁵¹. Additionally, we take $J_0^\perp = 0.3$ meV, $d = 7$ Å, and $a = 4$ Å, aligned with typical values observed in diverse vdW magnetic materials⁵⁶. We use the twist angle $\theta = 1.61^\circ$, which results in a moiré supercell with 5044 sites. These parameter values are utilized uniformly throughout this study unless explicitly specified.

The moiré superlattice of the twisted bilayer encompasses various local stacking patterns, such as AA, AB, and BA, within its supercell (Figure 2a). This stacking modulation leads to diverse spin alignments between the top and bottom layers. Two characteristic alignment patterns emerge:

$$\begin{aligned} \text{A-type Néel order: } \mathbf{N}_i^t \cdot \mathbf{N}_i^b &= -1, \\ \text{B-type Néel order: } \mathbf{N}_i^t \cdot \mathbf{N}_i^b &= +1. \end{aligned} \quad (3)$$

Here, \mathbf{N}_i^t and \mathbf{N}_i^b represent the Néel vectors on the top and bottom layers, respectively, defined as:

$$\mathbf{N}_i^{t,b} = \frac{\mathbf{S}_{i,A}^{t,b} - \mathbf{S}_{i,B}^{t,b}}{|\mathbf{S}_{i,A}^{t,b} - \mathbf{S}_{i,B}^{t,b}|}. \quad (4)$$

In the AA stacking regions (red patches in Figure 2a), the A-type order predominates since spins on the same sublattice in the top and bottom layers (e.g., $\mathbf{S}_{i,A}^t$ and $\mathbf{S}_{i,A}^b$ for the sublattice A) are coupled through the AFM coupling J_{ij}^\perp , as illustrated in the left panel of Figure 2b. Conversely, the AB stacking regions (blue patches in Figure 2a) favor the B-type order, as $\mathbf{S}_{i,A}^t$ and $\mathbf{S}_{i,B}^b$ are primarily coupled, while $\mathbf{S}_{i,B}^t$ and $\mathbf{S}_{i,A}^b$ remain effectively decoupled due to their large separations, as depicted in the middle panel of Figure 2b. Similarly, the BA stacking regions (cyan patches in Figure 2a) prefer a parallel alignment with similar considerations, as shown in the right panel of Figure 2b. We illustrate the intricate coexistence of these two orders using a map of the local interlayer exchange energy $J_i^\perp = \sum_j J_{ij}^\perp \mathbf{S}_i^t \cdot \mathbf{S}_j^b$, computed

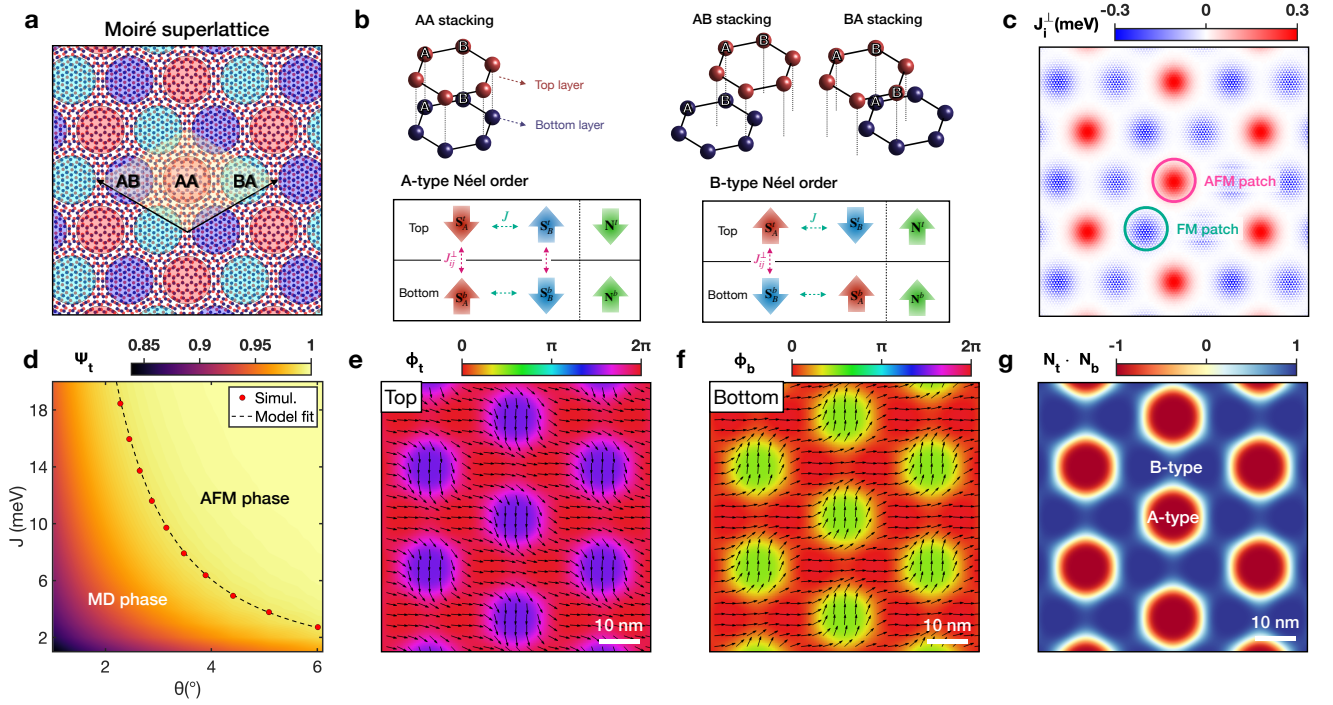


FIG. 2. **Antiferromagnetic domain array.** **a** Moiré superlattice for a twist angle of $\theta = 5.08^\circ$. Colored circles highlight distinct local stacking patterns: AA (red), AB (blue), and BA (cyan). The yellow rhombus and black arrows denote the unit cell and lattice vectors of the moiré superlattice, respectively. **b** Schematic illustration depicting different local spin configurations (A-type and B-type Néel orders) preferred in each stacking order. Here, red and blue arrows represent spins on the A and B sublattice, respectively. Green arrows depict Néel vectors in each layer. **c** Interlayer exchange energy map (J_i^\perp) within the B-type order. Here, red and blue colors indicate the preference for the A-type and B-type orders, respectively. **d** Zero temperature magnetic phase diagram as a function of twist angle (θ) and intralayer nearest-neighbor exchange interaction (J), displaying AFM and magnetic domain (MD) phases. The order parameter Ψ_t is defined as $\Psi_t = \frac{1}{N_t} |\sum_i \mathbf{N}_i^t|$ (\mathbf{N}_i^t : a Néel vector on each i -site, N_t : the number of sites on the top layer), where $\Psi_t = 1$ indicates the AFM phase, and $\Psi_t < 1$ signifies the MD phase. The markers depict the boundary between the two phases. The dashed line represents a fitting curve defined as $J = 162/\theta^2$. **e-g** AFM domain array configuration of the MD phase. In **e-f**, the color scales denote the phase angles ($\phi_{t,b}$) of the normalized Néel vectors $\mathbf{N}_{t,b} = (\cos \phi_{t,b}, \sin \phi_{t,b}, 0)$ in the top and the bottom layers, respectively. The arrows illustrate the direction of the Néel vectors in the plane. In **g**, the relative orientation of the Néel vectors between the two layers ($\mathbf{N}_t \cdot \mathbf{N}_b$), where red (blue) represents the A-type (B-type) Néel order.

for the B-type Néel order where $\mathbf{S}_{i,A}^t = \mathbf{S}_{i,A}^b = (1, 0, 0)$ and $\mathbf{S}_{i,B}^t = \mathbf{S}_{i,B}^b = (-1, 0, 0)$. The resulting map, presented in Figure 2c, showcases three distinct local regions: (i) “AFM patches” preferring the A-type order, as indicated by their AFM coupling character between two Néel vectors (i.e., $J_i^\perp > 0$), (ii) “FM patches” preferring the B-type order, as indicated by their FM coupling character (i.e., $J_i^\perp < 0$), and (iii) a neutral intermediate region lacking any specific preferred order, exhibiting negligible coupling (i.e., $J_i^\perp \approx 0$).

Our atomistic spin simulations on Eq. (1), conducted using an iterative optimization method^{47,54,55}, reveal a zero temperature magnetic phase diagram shown in Figure 2d (for detailed methods, refer to the Methods). This diagram displays two distinct magnetic phases: AFM and magnetic domain (MD) phases. The AFM phase displays a uniform spin configuration characterized by the B-type Néel order. In contrast, the MD phase exhibits a nonuniform configuration (Figure 2e-g), where the A-type Néel

order emerges within each AFM patch, forming circular-shaped domains, whereas the B-type Néel order persists outside these patches (Figure 2g). We term this spin configuration an “AFM domain array,”⁴⁷ attributed to the AFM-order-like configuration (i.e., antiparallel alignment of the Néel vectors between the two layers) within these domains that are arranged in an array pattern.

The AFM domain array configuration minimizes J_i^\perp across both the AFM and FM patch regions. This contrasts with the uniform AFM configuration, which only achieves low energy within the FM patches, leaving the AFM patches with higher energy. Our finding reveals that this energy reduction outweighs an increase from the domain wall energy, leading to an energy-minimized ground state configuration (for detailed information, refer to the Supplementary Information). A previous effective continuum model calculation suggests that the lowered interlayer exchange energy and domain wall energy are given by $\Delta E_{\text{inter}} \sim -\bar{J}_\perp \theta^{-2}$ and

$\Delta E_{\text{intra}} \sim +J$, respectively, where \bar{J}_{\perp} denotes the average value of J_i^{\perp} within an AFM patch^{47,54,55}. Notably, $|\Delta E_{\text{inter}}|$ outweighs $|\Delta E_{\text{intra}}|$ in a small twist angle regime ($\theta \leq \theta_c \sim \sqrt{\bar{J}_{\perp}/J}$). Furthermore, the formula $\theta_c = C\sqrt{\bar{J}_{\perp}/J}$ fits well the observed phase boundary with the parameters $\bar{J}_{\perp} = 0.3$ meV and $C = 23.24$ (the dashed line in Figure 2d). Consequently, the AFM domain array of the MD phase becomes a ground state in this small twist angle regime.

Meron Kekulé lattice. We demonstrate that the AFM domain array, depicted in Figure 2e–g, can accommodate merons as topological defects around its domain boundary, leading to a Meron Kekulé lattice. Figure 3 presents a stable spin configuration obtained through the relaxation of a random initial configuration. On the top layer, the Néel vectors exhibit six-fold in-plane swirling textures within a supercell, which are labeled by $M_1, M_2, M_3, \bar{M}_1, \bar{M}_2,$ and \bar{M}_3 (Figure 3a). The vorticity density of these textures is computed as⁵⁷:

$$v(x, y) = \frac{1}{\pi} \hat{z} \cdot (\partial_x \mathbf{N}(x, y) \times \partial_y \mathbf{N}(x, y)), \quad (5)$$

where $\mathbf{N}(x, y)$ represents the normalized interpolation of the Néel vectors in the top layer. The resulting map for $v(x, y)$, presented in Figure 3c, displays positive and negative values for (M_1, M_2, M_3) and $(\bar{M}_1, \bar{M}_2, \bar{M}_3)$, respectively, identifying the former as vortices and the latter as antivortices. Furthermore, $v(x, y)$ is locally integrated around each core region: $V = \int dx dy v(x, y)$ ⁵⁷, yielding winding numbers $V \approx +1$ and $V \approx -1$ for each group, confirming their vortex and antivortex nature.

The six vortices exhibit out-of-plane polarization in their core regions (Figure 3a), indicating that they carry an additional topological number defined in three-dimensional spin space, known as a skyrmion number. The local density profile for the skyrmion number is calculated as^{11,12}:

$$q(x, y) = \frac{1}{4\pi} \mathbf{N}(x, y) \cdot (\partial_x \mathbf{N}(x, y) \times \partial_y \mathbf{N}(x, y)). \quad (6)$$

The resulting map for $q(x, y)$, depicted in Figure 3d, demonstrates nonvanishing skyrmion densities with sign alternation for each core. These densities are locally integrated around each core region: $Q = \int dx dy q(x, y)$, yielding skyrmion numbers $Q \approx -1/2$ for the vortices and $Q \approx +1/2$ for the antivortices (for detailed methods, refer to the Methods). These half-skyrmion number characteristics identify (M_1, M_2, M_3) as merons and $(\bar{M}_1, \bar{M}_2, \bar{M}_3)$ as antimerons^{11,12,58}

The cores of the merons and antimerons form six vertices of a hexagon along the boundary of the AFM patch, with each pair, (M_1, \bar{M}_1) , (M_2, \bar{M}_2) , and (M_3, \bar{M}_3) , positioned oppositely among these vertices (Figure 3a). In this arrangement, the merons cancel out their swirling textures away from the cores, maintaining a localized configuration within a supercell. We refer to this distinctive local configuration as a ‘‘Meron hexad.’’ Despite

its intricate texture, the Meron hexad attains an AFM domain array configuration that minimizes interlayer exchange energy across the bulk region, including both FM and AFM patches (Figure 3e). This is achieved through two key mechanisms: (i) a 180° rotation of the Néel vectors across FM and AFM patches in the top layer facilitated by the hexagonal alignment of the meron cores around the AFM patch (Figure 3a) and (ii) a nearly uniform alignment of Néel vectors with a slight tilt in opposing directions between FM patches in the bottom layer (Figure 3b). Consequently, the Meron hexad attains a minimized energy (e.g., -1.5176 meV per spin for the configuration presented in Figure 3), comparable to that of the MD state (e.g., -1.5128 meV per spin for the configuration presented in Figure 2e–f). Our findings reveal that the small energy gap between the two states primarily stems from the core energy due to intralayer exchange interactions. Further details can be found in the Supplementary Information.

When replicated across multiple supercells to establish an energy-minimized configuration, Meron hexads form a regular triangular lattice that overlaps with the underlying moiré superlattice. However, the constituent meron cores of the Meron hexads create a more intricate pattern, where two nearest-neighbor meron cores from the same Meron hexad have a shorter distance than those two from adjacent Meron hexads (Figure 3a). This distorted structure is often referred to as a Kekulé lattice with a Kekulé-O pattern in the literature²⁸. Thus, we term this distorted meron lattice a ‘‘Meron Kekulé lattice (MK).’’ The Kekulé structure of the MK state is characterized by two key length parameters: the intracell bond length within the same Meron hexad (l) and the intercell bond length across different Meron hexads ($l' = L - 2l$), with L representing the lattice constant of the moiré superlattice (Figure 4a). The distinction between l and l' indicates the deviation from the conventional honeycomb lattice, giving rise to an alternative Kekulé structure, as schematically illustrated in Figure 4a. To quantify this deviation, we introduce a dimensionless constant λ , referred to as the ‘‘Kekulé constant.’’

$$\lambda = \frac{l' - l}{L} = 1 - \frac{3l}{L}. \quad (7)$$

If $\lambda = 0$, the meron lattice aligns with a regular honeycomb lattice. Conversely, if $\lambda \neq 0$, it corresponds to a Kekulé lattice. Typically, l is less than l' , leading to $\lambda > 0$ (e.g., $\lambda = 0.19$ for the meron lattice configuration in Figure 3).

Three length parameters (l , l' , and L) relevant to the MK state are primarily influenced by specific characteristics of the AFM patch, including its spatial size (r) and interlayer exchange coupling strength within the patch. The minimization of interlayer exchange energy favors the alignment between l and r , as having $l \approx r$ facilitates an energy-minimized AFM domain array configuration. Conversely, other aspects in the spin model, such as intralayer exchange interactions, interact with the interlayer exchange coupling of the AFM

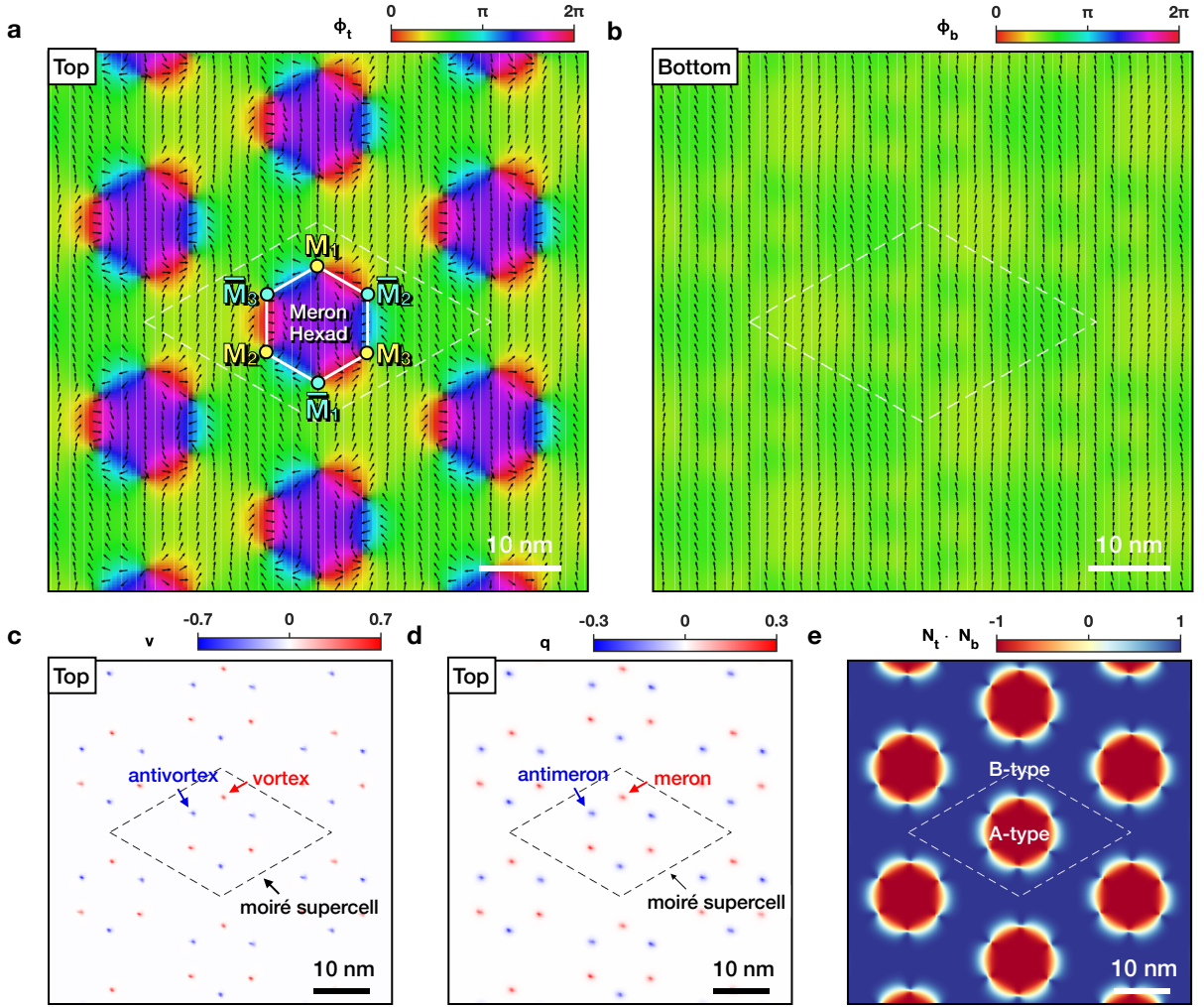


FIG. 3. **Meron Kekulé lattice (MK) configuration.** **a** Néel vectors on the top layer (N_t), showing three merons (M_1, M_2, M_3) and three antimerons ($\bar{M}_1, \bar{M}_2, \bar{M}_3$). **b** Néel vectors on the bottom layer (N_b), displaying almost homogeneous alignment. In **a–b**, the color scales denote the phase angles ($\phi_{t,b}$) of the normalized Néel vectors $\mathbf{N}_{t,b} = (\sin \theta_{t,b} \cos \phi_{t,b}, \sin \theta_{t,b} \sin \phi_{t,b}, \cos \theta_{t,b})$ in the top and the bottom layers, respectively. The black color denotes the out-of-plane component in the direction perpendicular to the plane (i.e., $N_t = (0, 0, 1)$). The arrows depict the interpolation of the in-plane components of the Néel vectors. **c** Vortex density (v) map corresponding to **a**, with red (blue) color indicating a positive (negative) winding number. **d** Skyrmion density (q) map corresponding to **a**, with red (blue) color indicating a positive (negative) skyrmion number. **e** The relative orientation of the Néel vectors between the two layers ($N_t \cdot N_b$), with blue (red) indicating parallel (antiparallel) alignment. In each panel, the dashed line depicts a supercell.

patch, potentially causing deviations from $l = r$. Thus, there exists an intriguing possibility that by manipulating various magnetic interactions in twisted antiferromagnets—represented by parameters like A/J , J_0^\perp/J , θ , α , d/a in our spin model—one can generate diverse Meron Kekulé lattices characterized by different values of l , l' , and L .

One straightforward avenue is to alter the twist angle (θ), which leads to the expansion of L proportionally to $L \approx \sqrt{3}a/\theta$ (θ : in radian). This expansion enlarges local AA stacking structures, inducing corresponding expansions in AFM patches. We observe that r expands at a rate commensurate with L (i.e., $r \propto L$), as shown by

the red line in Figure 4**b**. The r expansion results in an increase in l , which is directly correlated with r , and subsequently l' through the relation $l' = L - 2l$. However, the expansion rates of l and l' do not precisely overlap with that of L (the blue and green lines in Figure 4**b**, respectively). Their linear behaviors are well-captured by the fitting lines: $r = 0.28L + 0.05$, $l = 0.31L - 1.04$, and $l' = 0.38L + 2.09$, respectively. As a result, the expansion of L results in the modulation of λ (the inset in Figure 4**b**). It's worth mentioning that the discrete alternation of l and l' here originates from the discontinuous nature of the underlying honeycomb lattice, while the continuous behavior of r is attributed to our determina-

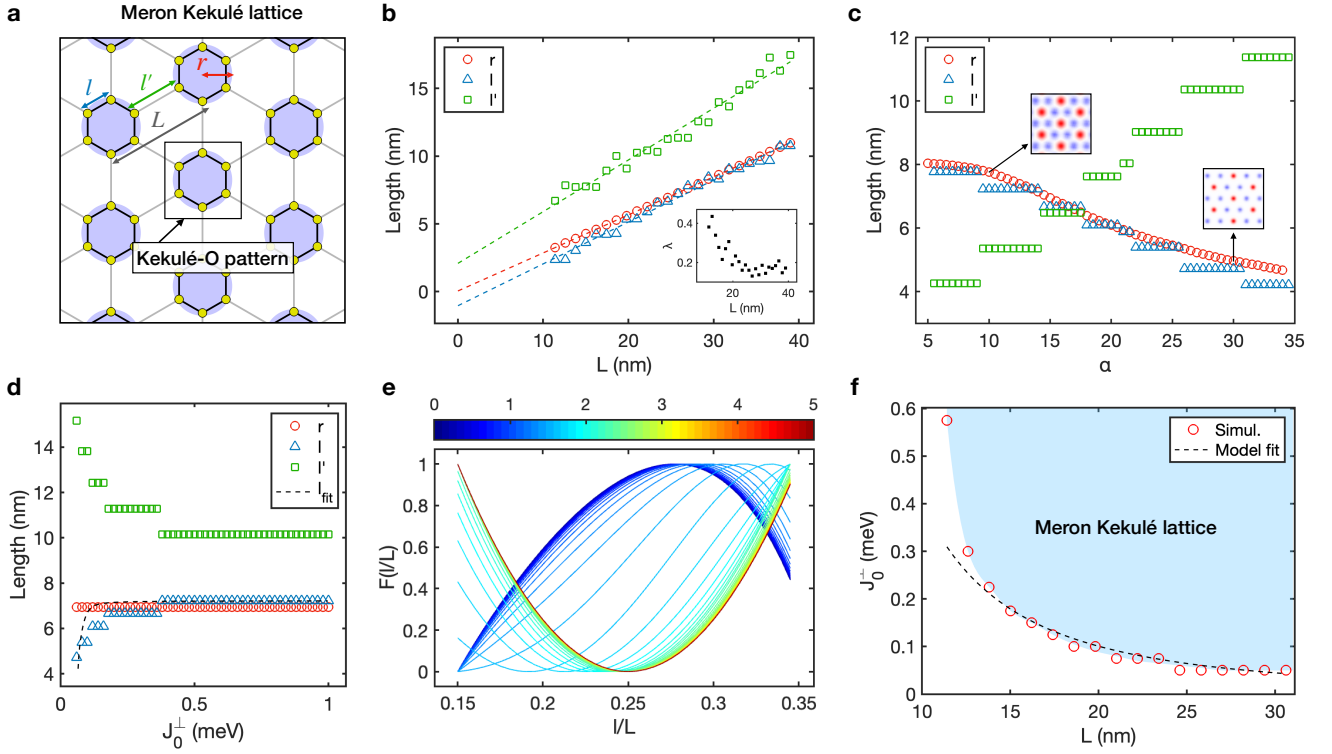


FIG. 4. Manipulation of the Kekulé structure through parameter adjustments. **a** Schematic illustration of the Meron Kekulé lattice structure. Yellow dots denote the position of the meron cores. Black lines denote intracell bonds between meron cores within a Meron hexad, while light gray lines denote intercell bonds between meron cores across different Meron hexads. l and $l' = l - 2L$ denote the intracell and intercell bond lengths, respectively. r denotes the size of AFM patches marked by purple circles. **b–d** Manipulation of the Kekulé lattice structure through three different parameters: **b** the moiré superlattice size (L), **c** the decay rate parameter of interlayer exchange interactions J_{ij}^\perp (α), and **d** the maximum strength of J_{ij}^\perp (J_0^\perp). In **b**, the inset shows the value of the Kekulé constant ($\lambda = \frac{l'-l}{L}$). The dashed lines represent empirical fitting curves. In **c**, the insets display J_{ij}^\perp for $\alpha = 10$ (left) and $\alpha = 30$ (right), respectively. The same color scale used in Figure 2c is applied in the insets. In **d**, the dashed line represents the fitting curve for the l values. **e** Effective energy function $E(l)$ for the MK state, plotted in a normalized form: $F(l/L) = \frac{E(l) - \min[E(l)]}{\max[E(l)] - \min[E(l)]}$. Here, ‘min’ and ‘max’ indicate the minimum and maximum values, respectively. Different colors indicate distinct values of $\log_{10}(p)$, where p represents the dimensionless ratio between the Coulomb interactions and the moiré field, which represent the two effective interactions influencing merons in the effective model. The parameter $r/L = 0.25$ is used. **f** Illustration of the stabilization condition of the MK state as a function of L and J_0^\perp . The MK state is stable in the blue region while unstable in the devoid region. The markers represent simulation data points, while the dashed line is a fitting curve defined as $J_0^\perp = 40/L^2$.

tion of the AFM patch through the interpolation of the interlayer exchange energy map. For detailed methods for r determination, refer to the Supplementary Information.

Alternatively, the adjustment of r can be achieved by modifying the decay rate parameter of the interlayer exchange coupling (α), as illustrated in Figure 4c. In this approach, r can be continuously decreased by increasing α (the red line in Figure 4c). This leads to the corresponding contraction of l with the alignment between r and l (the blue line in Figure 4c). Here, the decrease of r through the increase of α is attributed to a significant suppression of J_{ij}^\perp for a large value of $|\mathbf{r}_{ij}^{tb}|$ away from the center of an AFM patch. Similarly, reducing the ratio d/a also reduces r and contracts l (for detailed analysis, refer to the Supplementary Information). It’s worth

mentioning that within these two scenarios, r and l can be adjusted by keeping L intact, in contrast to the former approach of adjusting θ .

Instead of altering r , one can manipulate l by adjusting the ratio between the strengths of the interlayer exchange interactions (J_0^\perp) and intralayer exchange interactions (J). As illustrated in Figure 4d, an increase in J_0^\perp/J initially leads to an augmentation of l . However, as J_0^\perp/J becomes significant, l reaches its maximum value $l_{\max} \approx r$. Further changes in J_0^\perp/J do not affect l thereafter. We attribute this intricate behavior to the interplay between two magnetic interactions influencing merons: (i) attractive Coulomb interactions between merons and antimerons with opposite vorticities⁵⁹, induced by the intralayer exchange interactions, and (ii) an effective moiré field generated by the bottom layer

through interlayer exchange interactions⁴⁷. The former interaction tends to reduce l to minimize the Coulomb energy of meron-antimeron pairs. In contrast, the latter interaction favors $l = r$ to minimize the field energy associated with the interlayer exchange energy. We posit that the interplay between these two mechanisms, quantified by the ratio of the two couplings J_0^\perp/J , determines the precise equilibrium positions of the meron cores at a specific l , leading to the observed modulation of l .

To elucidate the interplay between the Coulomb interactions and the moiré field, we utilize an energy function derived from an effective continuum model (for the derivation, refer to the Supplementary Information). This energy function is expressed as:

$$E(l) = C_1 J \ln \left[\sqrt{2l/3L} \frac{(1 - (l/L)^6)^2 (1 - (2l/L)^6)}{(1 + (\sqrt{3}l/L)^6)^2} \right] + \frac{C_2 J_0^\perp}{a^2} (l - r)^2. \quad (8)$$

Here, the first term describes the Coulomb interactions ranging up to the nearest-neighbor supercells, and the second term represents the moiré field. The constants C_1 and C_2 are numerical factors on the order of unity. To represent the relative strengths of the two interactions, we introduce a dimensionless ratio: $p = (2J_0^\perp/J)(C_2/C_1)(L^2/a^2)$, where a small p value indicates that the Coulomb interactions dominate over the moiré field, and vice versa. We observe that when p is small, $E(l)$ displays concave characteristics throughout all l values (Figure 4e). In contrast, when p is large, $E(l)$ exhibits a local minimum near $l \approx r$ (e.g., $l \approx 0.25L$ for $r = 0.25L$ in Figure 4e), which stabilizes the MK state by positioning the meron cores at this location. In this regime, we determine the precise location of the meron cores by minimizing $E(l)$ with respect to l . Our analysis showcases that the resulting l_* captures the qualitative features of the observed l values (as depicted by the dashed lines in Figure 4d), suggesting the applicability of this effective model. For the detailed fitting method, refer to the Methods.

The effective potential $E(l)$ provides insights into the underlying mechanism supporting the stability of merons within the MK state. In conventional magnets, merons tend to be unstable due to Coulomb interactions, undergoing pair annihilation during energy relaxation processes. However, in our twisted magnets, the moiré field may mitigate this instability by confining the meron cores near the AFM domain boundary. Any deviation of the cores from this boundary results in an energy penalty, preventing pair annihilation. This protective effect of the moiré field is notably strengthened with increased interlayer exchange coupling or reduced twist angles, suggesting that the stabilization of the MK state occurs in conditions favoring strong intralayer exchange or small twist angles. Our numerical simulations validate this trend, aligning with predictions from the effective model (illustrated by the dashed line in Figure 4f). Consequently,

θ (°)	α	d/a	J_0^\perp	l (nm)	l' (nm)	L (nm)	λ
1.61	15	1.75	0.3	6.66	11.28	24.60	0.19
1.05	15	1.75	0.3	10.74	16.32	37.80	0.15
2.28	15	1.75	0.3	4.23	8.94	17.40	0.27
1.61	8	1.75	0.3	7.77	9.06	24.60	0.05
1.61	25	1.75	0.3	5.39	13.82	24.60	0.34
1.61	15	1.40	0.3	6.09	12.42	24.60	0.26
1.61	15	2.00	0.3	7.22	10.16	24.60	0.12
1.61	15	1.75	0.1	5.38	13.83	24.60	0.34
1.61	15	1.75	0.5	7.22	10.15	24.60	0.12

TABLE I. Examples of Kekulé structures (characterized by four parameters l, l', L , and λ) in the MK state with various parameters. The first row corresponds to the MK state shown in Figure 3. Subsequent rows illustrate the changes in the Kekulé structures induced by the variations in the twist angle (θ), the decay rate of interlayer exchange coupling (α), the lattice length ratio (d/a), and the interlayer exchange coupling strength (J_0^\perp) from the first-row case. Here, a and d denote the nearest-neighbor distance within the same layer and the perpendicular interlayer distance, respectively. a is set to 4 Å.

we posit that adjusting the twist angle or interlayer exchange coupling strength can effectively stabilize the MK state.

Based on our theoretical investigations, as depicted in Figure 4, we propose a methodology for realizing diverse Meron Kekulé lattice structures. Specified examples of such structures are illustrated in Table I. Firstly, one can create Meron Kekulé lattices at various length scales (l, l' , and L) by manipulating the size of the moiré superlattice (L) through adjustments in the twist angle (θ)^{60–62}. Another method involves modifying the specifics of interlayer exchange coupling ($\alpha, d/a$, and J_0^\perp/J), which enables the manipulation of l and l' while keeping L constant. Experimentally, the latter approach can be implemented using different antiferromagnetic materials or external controls such as gate voltage, intercalation, adsorption, strain, or surface adsorption⁶³. The resulting Kekulé lattices display a wide range of distortion, as indicated by λ values ranging from 0.05 to 0.34. This high degree of adaptability underscores a unique characteristic of the Meron Kekulé lattice, providing a promising avenue for experimental validation of its existence.

In real magnetic systems, the adaptability of the Meron Kekulé lattice might be limited by its stability conditions. For instance, our analysis reveals that insufficient single-ion anisotropy energy results in the decay of the MK state into the MD state through pair annihilation. Further details are available in the Supplementary Information. Additionally, it is crucial to consider material-specific properties that can impose constraints. For example, we assume that material values of α might range from 5 to 30, where $\alpha = 5$ corresponds to $J_{ij}^\perp/J_0^\perp = 0.47$ at the second-nearest neighbor distance between the top and bottom layers in the AA stacking,

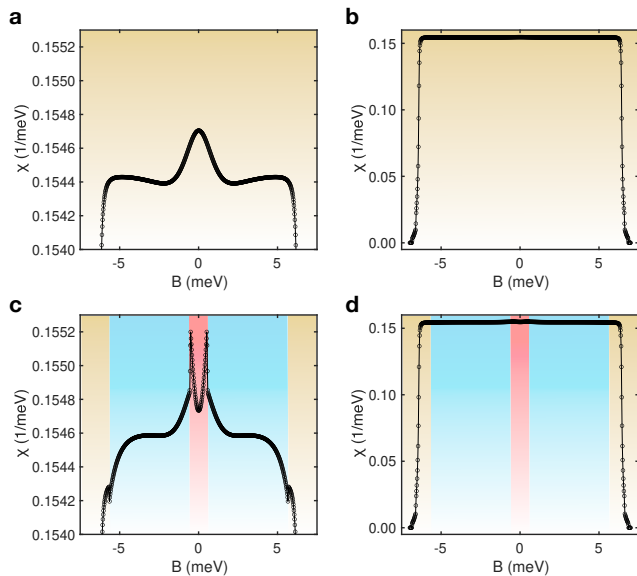


FIG. 5. **a** Magnetic susceptibility ($\chi = dM/dB$) of the MD state with respect to the out-of-plane magnetization (M) as a function of an external magnetic field in the out-of-plane direction (B). **b** Zoom-out view of **a**. In **a–b**, the yellow color highlights the persistence of the MD state. **c** Magnetic susceptibility (χ) of the MK state. Different colors indicate three different magnetic states: MK state (red), vortex state (blue), and MD state (yellow). **d** Zoom-out view of **c**.

while $\alpha = 30$ yields $J_{ij}^\perp/J_0^\perp = 0.01$ at the same distance. This range aligns with previous ab-initio calculations for monolayer CrBr₃ on substrate MnPSe₃, estimating $\alpha \approx 10$ with $d/a \approx 1.89$ ⁵¹. Moreover, typical van der Waals magnetic materials exhibit $d/a \approx 1$ to 2 and $J_0^\perp/J \approx 0.1$ to 0.3⁵⁶. These material-specific values serve as constraining factors that potentially limit the adaptability of the Meron Kekulé lattice.

It is also worth noting that, unlike in our theoretical framework, the parameters that characterize the spin system may not be independently manipulable in real magnetic systems under experimental constraints. One plausible scenario is that reducing d may lead to a simultaneous decrease in d/a and an increase in J_0^\perp/J . In this context, our analysis indicates a potential nonmonotonic behavior of l ; it may initially show a decreasing trend due to the high value of J_0^\perp/J , as illustrated in Figure 4d, followed by an increasing trend due to the enlargement of r , as suggested by Figure 4b. Predicting this behavior accurately presents an intriguing prospect for future research, requiring precise modeling of interlayer magnetic coupling through ab-initio calculations^{37,51,54,64–66}. While this task is beyond the scope of the current study, we emphasize that the observed susceptibility of Kekulé structures holds promise for future experimental validation.

To investigate a potential means to distinguish the MD and MK states by bulk measurements, we analyze the magnetic response of the MD and MK states to external

magnetic fields, incorporating the Zeeman term defined as:

$$H_{\text{Zeeman}} = - \sum_{l=t,b} \sum_i \mathbf{B} \cdot \mathbf{S}_i^l, \quad (9)$$

where $\mathbf{B} = B\hat{\mathbf{z}}$ denotes external magnetic fields in the out-of-plane magnetization. The initial MD and MK states, as presented in Figures 3 and 4, are relaxed under external magnetic fields with continuously varying strength B . From the relaxed spin configurations for each state, the magnetic susceptibility, defined as $\chi \equiv dM/dB$, is calculated as a function of B , where M is the average magnetization in the out-of-plane magnetization, defined as $M = \frac{1}{N} \sum_{i,l} \mathbf{S}_i^l \cdot \hat{\mathbf{z}}$. Figure 5a–b presents the magnetic susceptibility χ of the MD state. Starting from the zero-field point $B = 0$, χ initially decreases as $|B|$ increases, while it shows an upturn in $|B| > 2.22$ meV, exhibiting shoulder-like features around $|B| = 4.88$ meV (Figure 5a). Beyond these shoulders, χ sharply drops, and subsequently vanishes at $|B| > B_{\text{sat.}} = 6.86$ meV (Figure 5b), where the magnetization saturates at $|M| = 1$. We observe that despite this intricate behavior of χ , the MD state persists throughout the entire field range, which is highlighted by the same yellow color.

Figure 5c–d presents the magnetic susceptibility χ of the MK state. In the low-field regime ($|B| < B_{c1} = 0.52$ meV; colored by red), χ exhibits an increasing tendency with $|B|$ in contrast to the MD state. This behavior is attributed to the canted spin configurations in the core region that enhance the magnetization induced by the field. However, entering into the intermediate-field regime ($B_{c1} \leq |B| < B_{c2} = 5.62$ meV; colored by blue), χ undergoes a sharp drop and subsequently exhibits a decreasing tendency similar to the MD state. Our findings reveal that at the threshold $|B| = B_{c1}$, the spin flipping occurs in the perpendicular direction for spins with out-of-plane components opposite to the field direction. The resulting state maintains in-plane swirling textures while lacking out-of-plane components in their Néel vectors. Consequently, this state retains only vorticities but loses half-skyrmion numbers characteristics, thus being named a “vortex state” (for the detailed spin configuration and skyrmion numbers analysis, refer to the Supplementary Information). Finally, upon entering the high-field regime ($|B| \geq B_{c2}$; colored by yellow), the vortex state transitions into the MD state through the annihilation of meron-antimeron pairs. At this regime, χ aligns with that of the MD state, as shown in the yellow region in Figure 5d. We highlight the two anomalous discontinuities at the transition points ($|B| = B_{c1}$ and $|B| = B_{c2}$), which are absent in the MD state, as discernible signatures of the formation of merons in the MK state. We propose experimental measurement of these anomalies to validate the Meron Kekulé lattice.

Despite our specific focus on the configuration depicted in Figure 3, the MK state can manifest in a diverse array of 2^6 potential configurations, each defined by two possible vorticities ($p = \pm 1$) for the six meron cores within

a moiré supercell. Among these configurations, only 2⁵ could exhibit variations in energy levels since global polarity reversal has no impact on the energy state. Our analysis indicates that despite the multitude of configurations, they maintain almost identical energy levels, deviating by less than 10⁻⁶ percentage from each other. Additionally, completely interchanging the positions of vortices and antivortices introduces a factor of 2, while swapping the top and bottom layers introduces another factor of 2, resulting in a total of $G = 2^8$ potential variants for the MK state, all possessing the same energy level. This suggests that each supercell can assume one of the G configurations with nearly identical energies. Consequently, a system comprising N_s supercells can present a total of G^{N_s} distinct configurations, underscoring the vast diversity and potential intricacy of the MK state. For a more detailed analysis, refer to the Supplementary Information.

The configurational diversity of the MK state suggests that it might be more favorable at finite temperatures compared to the ground MD state. To evaluate this, we calculate the expected occupation number of Meron hexads in each moiré supercell, denoted by f_{MH} , at temperature T . Considering two possibilities, the MD and MK configurations for each supercell, we express f_{MH} as: $f_{\text{MH}} \simeq \frac{G e^{-E_{\text{MK}}/k_B T}}{e^{-E_{\text{MD}}/k_B T} + G e^{-E_{\text{MK}}/k_B T}}$, where E_{MK} and E_{MD} represent the energies of the MK and MD states from a single supercell, respectively. In this calculation, we assume the energy of each supercell is independent of the presence or absence of a Meron hexad (an approximation that might hold unless a significant number of Meron hexads occupy the supercells). By utilizing the calculated value, $E_{\text{MK}} - E_{\text{MD}} = 21.44$ meV at $\theta = 1.02^\circ$, we determine $f_{\text{MH}} = 0.32$ at $T = 40$ K. Similarly, for $E_{\text{MK}} - E_{\text{MD}} = 9.29$ meV at $\theta = 0.50^\circ$, estimated from the fitting, we derive $f_{\text{MH}} = 0.49$ at $T = 20$ K (for further details, refer to the Supplementary Information). These results imply that achieving the MK state at a finite temperature is feasible by either increasing the temperature or adjusting the twist angle at a small value⁶⁷. During our investigations, we also observed an alternative meron configuration characterized by either a single meron pair or double meron pairs in one of the two layers. In realistic settings, these configurations might appear in some of the supercells, acting as defects in the Meron Kekulé lattice. Investigating the effect of these defects presents an intriguing prospect for future research.

Discussion

We highlight that the stabilizing mechanism for the Meron Kekulé lattice is solely attributed to twist-induced lateral modulation of atomic stacking structures, irrespective of detailed characteristics in the interlayer exchange coupling. This contrasts with previous twist-engineering approaches for achieving topological spin textures, such as skyrmions^{53-55,64,65,68-71} and merons⁴⁷, which relied on stacking-dependent interlayer magnetism

confined to the CrX₃ family (X = I, Cl, Br)^{65,72-74}. Therefore, our approach presents an intriguing possibility for realizing topological spin textures in diverse vdW AFM materials^{56,75} independent of such material-specific properties.

We propose that our theory can be applied to CoPS₃, which exhibits two essential factors for achieving the Meron Kekulé lattice: AFM intralayer exchange interactions and easy-plane magnetic anisotropy. Another potential application lies in XPS₃ (X = Mn, Ni, Fe) and MnPSe₃, where their intrinsic easy-axis magnetic anisotropy can be potentially altered into easy-plane anisotropy through experimental control, such as strain, gate voltage, or surface adsorption⁷⁶⁻⁸⁰.

An intriguing research question to explore is how the formation of a Meron Kekulé lattice affects magnon band structures through its distorted lattice structure in vdW antiferromagnets. One potential outcome suggested by prior investigations is the creation of topological band structures by opening a band gap through hopping amplitude modulation⁴¹⁻⁴³. Furthermore, exploring phonon-like collective-excitation modes stemming from meron core vibrations within the Meron Kekulé lattice presents a compelling avenue for investigating topological band structures, similar to the approach used for lattice-forming skyrmion cores^{81,82}.

For experimental observations, we propose utilizing scanning magnetometry techniques with nitrogen-vacancy centers, as well as Lorentz transmission electron microscopy and magnetic transmission soft X-ray microscopy, to directly observe meron pairs ranging in size from 40 to 10 nm at different twist angles ($\theta = 0.5^\circ$ to 2°). Indirect measurements can involve detecting the anomalous multiple superlattice periodicity manifested by different bond lengths meron through neutron scattering experiments. Additionally, anomalous kinks in the magnetization curve, as observed in Figure 5, can offer valuable insights for such indirect measurements, serving as an indication of the presence of merons.

Methods

Relaxation of spin configurations.

To achieve relaxed spin configurations, we employed an “iterative optimization method”^{47,54,55,83}. We initially generated random spin configurations represented by normalized vectors $\mathbf{n}_i = \mathbf{S}_i/|\mathbf{S}_i|$ for a classical spin vector \mathbf{S}_i at each i -th site. An effective magnetic field \mathbf{h}_i , acting on each \mathbf{S}_i , was computed as $\mathbf{h}_i \equiv \frac{\partial H[\{\mathbf{n}_i\}]}{\partial \mathbf{n}_i}$. Subsequently, we iteratively updated \mathbf{n}_i by subtracting \mathbf{h}_i from \mathbf{n}_i , resulting in a spin configuration with reduced magnetic energy at each iteration. The update rule is defined as:

$$\mathbf{n}_i^{(s+1)} = \frac{\mathbf{n}_i^{(s)} - c\mathbf{h}_i^{(s)}}{\left| \mathbf{n}_i^{(s)} - c\mathbf{h}_i^{(s)} \right|}, \quad (10)$$

where (s) denotes the iteration step, and c controls the update rate. The iteration proceeds until $\mathbf{h}_i^{(s)}$ becomes parallel to $\mathbf{n}_i^{(s)}$, indicating that further updates will not alter the spin configuration and ensuring minimal magnetic energy. To guarantee numerical convergence, we employed the condition $\frac{1}{N} \sum_i |\mathbf{h}_i^\perp| < 10^{-10}$, where $\mathbf{h}_i^\perp = \mathbf{h}_i - \mathbf{n}_i(\mathbf{n}_i \cdot \mathbf{h}_i)$. This convergence criterion aligns with the stability condition in the Landau-Lifshitz-Gilbert equation governing the magnetic dynamics. Throughout the iterative updates, we applied periodic boundary conditions to maintain consistency across the boundaries of the moiré unit cell.

Determination of the phase diagram.

To obtain the phase diagram presented in Figure 2d, we used random initial configurations denoted as $\{\mathbf{n}_i^{(0)}\} = \{(\frac{u_i}{n_i}, \frac{v_i}{n_i}, \frac{w_i}{n_i})\}$, where u_i , v_i , and w_i are random numbers within the range of $[-1, 1]$ and $n_i = \sqrt{u_i^2 + v_i^2 + w_i^2}$. These initial configurations were relaxed using an iterative optimization method to obtain the relaxed configuration $\{\mathbf{n}_i\}$. The ground state was identified as the lowest energy configuration among $\{\mathbf{n}_i\}$ for each parameter set (θ, J) . From the resulting ground states, the order parameters Ψ_l , defined as

$$\Psi_l = \left| \frac{1}{N_l} \sum_i N_i^l \right| \quad (11)$$

were calculated for each layer $l = t, b$. Here, N_l is the number of spins in each layer l . The AFM phase is characterized by $\Psi_t = \Psi_b = 1$, while the MD phase signifies $\Psi_t < 1$ and $\Psi_b < 1$. Ψ_t was presented in Figure 2d. It was found that the difference between Ψ_t and Ψ_b is less than 10^{-13} .

Computation of the vorticity and skyrmion densities.

To compute the vorticity and skyrmion density maps of the MK state, depicted in Figure 3c-d, we performed interpolation of the Néel vectors representing the spin configuration from the original honeycomb lattice to a square lattice consisting of N_{sq} sites. Subsequently, the vorticity and skyrmion densities were calculated using these interpolated Néel vectors via Eqs. (5) and (6), respectively, with $N_{\text{sq}} = 201^2$. This method yielded consistent values for vorticity and skyrmion numbers, as demonstrated by obtaining $V_1 = 0.9985$ and $Q_1 = -0.4926$ for the meron M_1 when employing $N_{\text{sq}} = 1,001^2$. These values closely align with the theoretical expectations of $V_1 = 1$ and $Q_1 = -1/2$. The positions of the meron cores, as depicted in Figure 4b-d, were identified based on the peak locations of these maps.

Determination of various Kekulé structures from different parameter sets.

To determine l of the MK state from different parameter sets, as presented in Figure 4b-d, we utilized various spin configurations characterized by different l values. These initial trial configurations were generated through the interpolation of the original MK state to attain diverse initial l/L values ranging from 0.2 to 1.2 with an interval of 0.02. Subsequently, for each parameter set, the initial configurations were relaxed through the iterative optimization method to obtain stable spin configurations that potentially possess different l . From the relaxed spin configurations, an energy profile of the MK state, $E_{\text{simul.}}(l)$, was computed as a function of l . $E_{\text{simul.}}(l)$ typically exhibits a convex behavior with a local minimum. The predominant MK states for each parameter set were selected based on the minimized energy configuration, and the l values were computed from these states. Similarly, the stabilization condition of the MK state, as presented in Figure 4f, was determined from the energy profile; the presence (absence) of the local minimum in this profile indicates the stable (unstable) nature of the MK state in each phase space. Further details are available in the Supporting Information.

Predictions made from the effective energy function.

To derive the fitting curve in Figure 4d, we identified a local minimum l_* of $E(l)$ in Eq. (8) by solving the equation $\frac{dE(l_*)}{dl} = 0$ under the constraint $\frac{d^2E(l_*)}{dl^2} > 0$. In the calculations, the parameters $J = 1$, $L = 24.60$, and $a = 0.4$ were used, and $r = 7.22$ were adopted from the simulation. The fitting parameter $C \equiv C_2/C_1 = 19.74$ was employed. The fitting curve in Figure 4f was derived from the formula $J_0^\perp = D/L^2$ where $D = \frac{pJa^2C}{2}$. In the fitting, the parameters $J = 1$, $a = 0.4$, and $p = 23.6$ were used, where the value of p was determined by the threshold value of p for the stabilization of the MK state as determined from our numerical investigations (further details are available in the Supporting Information). The fitting parameter C was estimated as $C = 21.33$, which is consistent with the estimation of $C = 19.74$ from Figure 4d.

ACKNOWLEDGEMENT

K.-M.K. would like to thank Chang-Hwan Yi and Beom Hyun Kim for sharing their insights. K.-M.K. was supported by the Institute for Basic Science in the Republic of Korea through the project IBS-R024-D1. S.K.K. was supported by Brain Pool Plus Program through the National Research Foundation of Korea funded by the Ministry of Science and ICT (2020H1D3A2A03099291) and National Research Foundation of Korea funded by the Korea Government via the SRC Center for Quantum Coherence in Condensed

-
- [1] T. Shinjo, T. Okuno, R. Hassdorf, K. Shigeto, and T. Ono, Magnetic vortex core observation in circular dots of permalloy, *Science* **289**, 930 (2000).
- [2] C. Phatak, A. K. Petford-Long, and O. Heinonen, Direct observation of unconventional topological spin structure in coupled magnetic discs, *Phys. Rev. Lett.* **108**, 067205 (2012).
- [3] S. Wintz, C. Bunce, A. Neudert, M. Körner, T. Strache, M. Buhl, A. Erbe, S. Gemming, J. Raabe, C. Quitmann, and J. Fassbender, Topology and origin of effective spin meron pairs in ferromagnetic multilayer elements, *Phys. Rev. Lett.* **110**, 177201 (2013).
- [4] A. Tan, J. Li, A. Scholl, E. Arenholz, A. T. Young, Q. Li, C. Hwang, and Z. Q. Qiu, Topology of spin meron pairs in coupled Ni/Fe/Co/Cu(001) disks, *Phys. Rev. B* **94**, 014433 (2016).
- [5] K. Shigeto, T. Okuno, K. Mibu, T. Shinjo, and T. Ono, Magnetic force microscopy observation of antivortex core with perpendicular magnetization in patterned thin film of permalloy, *App. Phys. Lett.* **80**, 4190 (2002).
- [6] X. Fu, S. D. Pollard, B. Chen, B.-K. Yoo, H. Yang, and Y. Zhu, Optical manipulation of magnetic vortices visualized in situ by lorentz electron microscopy, *Sci. Adv.* **4**, eaat3077 (2018).
- [7] B. Van Waeyenberge, A. Puzic, H. Stoll, K. W. Chou, T. Tylliszczak, R. Hertel, M. Fähnle, H. Brückl, K. Rott, G. Reiss, I. Neudecker, D. Weiss, C. H. Back, and G. Schütz, Magnetic vortex core reversal by excitation with short bursts of an alternating field, *Nature* **444**, 461 (2006).
- [8] A. Ruotolo, V. Cros, B. Georges, A. Dussaux, J. Grollier, C. Deranlot, R. Guillemet, K. Bouzehouane, S. Fusil, and A. Fert, Phase-locking of magnetic vortices mediated by antivortices, *Nat. Nanotechnol.* **4**, 528 (2009).
- [9] P. E. Roy, J. H. Lee, T. Trypiniotis, D. Anderson, G. A. C. Jones, D. Tse, and C. H. W. Barnes, Antivortex domain walls observed in permalloy rings via magnetic force microscopy, *Phys. Rev. B* **79**, 060407 (2009).
- [10] F. P. Chmiel, N. Waterfield Price, R. D. Johnson, A. D. Lamirand, J. Schad, G. van der Laan, D. T. Harris, J. Irwin, M. S. Rzechowski, C.-B. Eom, and P. G. Radaelli, Observation of magnetic vortex pairs at room temperature in a planar α -Fe₂O₃/Co heterostructure, *Nat. Mater.* **17**, 581 (2018).
- [11] X. Z. Yu, W. Koshibae, Y. Tokunaga, K. Shibata, Y. Taguchi, N. Nagaosa, and Y. Tokura, Transformation between meron and skyrmion topological spin textures in a chiral magnet, *Nature* **564**, 95 (2018).
- [12] N. Gao, S.-G. Je, M.-Y. Im, J. W. Choi, M. Yang, Q. Li, T. Y. Wang, S. Lee, H.-S. Han, K.-S. Lee, W. Chao, C. Hwang, J. Li, and Z. Q. Qiu, Creation and annihilation of topological meron pairs in in-plane magnetized films, *Nat. Commun.* **10**, 5603 (2019).
- [13] X. Lu, R. Fei, L. Zhu, and L. Yang, Meron-like topological spin defects in monolayer CrCl₃, *Nat. Commun.* **11**, 4724 (2020).
- [14] M. Augustin, S. Jenkins, R. F. L. Evans, K. S. Novoselov, and E. J. G. Santos, Properties and dynamics of meron topological spin textures in the two-dimensional magnet CrCl₃, *Nat. Commun.* **12**, 185 (2021).
- [15] R. Tomasello, E. Martinez, R. Zivieri, L. Torres, M. Carpentieri, and G. Finocchio, A strategy for the design of skyrmion racetrack memories, *Sci. Rep.* **4**, 6784 (2014).
- [16] S. Luo and L. You, Skyrmion devices for memory and logic applications, *APL Mater.* **9**, 050901 (2021).
- [17] W. Kang, Y. Huang, C. Zheng, W. Lv, N. Lei, Y. Zhang, X. Zhang, Y. Zhou, and W. Zhao, Voltage controlled magnetic skyrmion motion for racetrack memory, *Sci. Rep.* **6**, 23164 (2016).
- [18] W. Legrand, D. Maccariello, F. Ajejas, S. Collin, A. Vecchiola, K. Bouzehouane, N. Reyren, V. Cros, and A. Fert, Room-temperature stabilization of antiferromagnetic skyrmions in synthetic antiferromagnets, *Nat. Mater.* **19**, 34 (2020).
- [19] Y. Li, Q. Feng, S. Li, K. Huang, M. Ma, W. Gan, H. Zhou, X. Jin, X. Renshaw Wang, Y. Lu, W. S. Lew, Q. Lu, and F. Ma, An artificial skyrmion platform with robust tunability in synthetic antiferromagnetic multilayers, *Adv. Funct. Mater.* **30**, 1907140 (2020).
- [20] C. Chamon, Solitons in carbon nanotubes, *Phys. Rev. B* **62**, 2806 (2000).
- [21] C.-Y. Hou, C. Chamon, and C. Mudry, Electron fractionalization in two-dimensional graphenelike structures, *Phys. Rev. Lett.* **98**, 186809 (2007).
- [22] V. V. Cheianov, O. Syljuåsen, B. L. Altshuler, and V. Fal'ko, Ordered states of adatoms on graphene, *Phys. Rev. B* **80**, 233409 (2009).
- [23] S. Ryu, C. Mudry, C.-Y. Hou, and C. Chamon, Masses in graphenelike two-dimensional electronic systems: Topological defects in order parameters and their fractional exchange statistics, *Phys. Rev. B* **80**, 205319 (2009).
- [24] C. Weeks and M. Franz, Interaction-driven instabilities of a dirac semimetal, *Phys. Rev. B* **81**, 085105 (2010).
- [25] S. Kopylov, V. Cheianov, B. L. Altshuler, and V. I. Fal'ko, Transport anomaly at the ordering transition for adatoms on graphene, *Phys. Rev. B* **83**, 201401 (2011).
- [26] N. A. García-Martínez, A. G. Grushin, T. Neupert, B. Valenzuela, and E. V. Castro, Interaction-driven phases in the half-filled spinless honeycomb lattice from exact diagonalization, *Phys. Rev. B* **88**, 245123 (2013).
- [27] H. Mu, B. Liu, T. Hu, and Z. Wang, Kekulé lattice in graphdiyne: Coexistence of phononic and electronic second-order topological insulator, *Nano Lett.* **22**, 1122 (2022).
- [28] C. Gutiérrez, C.-J. Kim, L. Brown, T. Schiros, D. Nordlund, E. Lochocki, K. M. Shen, J. Park, and A. N. Pasupathy, Imaging chiral symmetry breaking from kekulé bond order in graphene, *Nat. Phys.* **12**, 950 (2016).
- [29] Y. Liu, C.-S. Lian, Y. Li, Y. Xu, and W. Duan, Pseudospins and topological effects of phonons in a kekulé lattice, *Phys. Rev. Lett.* **119**, 255901 (2017).
- [30] C. Bao, H. Zhang, T. Zhang, X. Wu, L. Luo, S. Zhou, Q. Li, Y. Hou, W. Yao, L. Liu, P. Yu, J. Li, W. Duan, H. Yao, Y. Wang, and S. Zhou, Experimental evidence of chiral symmetry breaking in kekulé-ordered graphene, *Phys. Rev. Lett.* **126**, 206804 (2021).

- [31] M. G. Scheer and B. Lian, Twistronics of kekulé graphene: Honeycomb and kagome flat bands, *Phys. Rev. Lett.* **131**, 266501 (2023).
- [32] T. Kawarabayashi, Y. Inoue, R. Itagaki, Y. Hatsugai, and H. Aoki, Robust zero modes in disordered two-dimensional honeycomb lattice with kekulé bond ordering, *Annal. Phys.* **435**, 168440 (2021), special Issue on Localisation 2020.
- [33] Y. Otsuka and S. Yunoki, Kekulé valence bond order in the hubbard model on the honeycomb lattice with possible lattice distortions for graphene, *Phys. Rev. B* **109**, 115131 (2024).
- [34] E. Andrade, R. Carrillo-Bastos, P. A. Pantaleón, and F. Mireles, Resonant transport in Kekulé-distorted graphene nanoribbons, *J. Appl. Phys.* **127**, 054304 (2020).
- [35] S. E. Freeney, J. J. van den Broeke, A. J. J. Harsveld van der Veen, I. Swart, and C. Morais Smith, Edge-dependent topology in kekulé lattices, *Phys. Rev. Lett.* **124**, 236404 (2020).
- [36] Y.-C. Jiang, T. Kariyado, and X. Hu, Higher-order topology in honeycomb lattice with y-kekulé distortions, *J. Phys. Soc. Jpn.* **93**, 033703 (2024).
- [37] P. Zhang, C. Wang, Y.-X. Li, L. Zhai, and J. Song, The transport properties of kekulé-ordered graphene p-n junction, *New J. Phys.* **25**, 113021 (2023).
- [38] Y. Mohammadi, Magneto-optical conductivity of graphene: Signatures of a uniform y-shaped kekulé lattice distortion, *ECS J. Solid State Sci. Technol.* **10**, 061011 (2021).
- [39] O. V. Gamayun, V. P. Ostroukh, N. V. Gnezdilov, I. Adagideli, and C. W. J. Beenakker, Valley-momentum locking in a graphene superlattice with y-shaped kekulé bond texture, *New J. Phys.* **20**, 023016 (2018).
- [40] X. Gao, L. Yang, H. Lin, L. Zhang, J. Li, F. Bo, Z. Wang, and L. Lu, Dirac-vortex topological cavities, *Nat. Nanotechnol.* **15**, 1012 (2020).
- [41] G. Wei, Z. Liu, L. Wang, J. Song, and J.-J. Xiao, Coexisting valley and pseudo-spin topological edge states in photonic topological insulators made of distorted kekulé lattices, *Photon. Res.* **10**, 999 (2022).
- [42] H. Huang, J. Chen, L. Mao, and R. Wang, Simultaneous pseudospin and valley topological edge states of elastic waves in phononic crystals made of distorted kekulé lattices, *J. Phys. Condens. Matter* **36**, 135402 (2023).
- [43] B. Xie, H. Liu, H. Cheng, Z. Liu, S. Chen, and J. Tian, Acoustic topological transport and refraction in a kekulé lattice, *Phys. Rev. Appl.* **11**, 044086 (2019).
- [44] D. Ma, Z. Fu, X. Sui, K. Bai, J. Qiao, C. Yan, Y. Zhang, J. Hu, Q. Xiao, X. Mao, W. Duan, and L. He, Modulating the electronic properties of graphene by self-organized sulfur identical nanoclusters and atomic superlattices confined at an interface, *ACS Nano* **12**, 10984 (2018).
- [45] U. Essmann and H. Träuble, The direct observation of individual flux lines in type ii superconductors, *Phys. Lett. A* **24**, 526 (1967).
- [46] S. Mühlbauer, B. Binz, F. Jonietz, C. Pfleiderer, A. Rosch, A. Neubauer, R. Georgii, and P. Böni, Skyrmion lattice in a chiral magnet, *Science* **323**, 915 (2009).
- [47] K.-M. Kim, G. Go, M. J. Park, and S. K. Kim, Emergence of stable meron quartets in twisted magnets, *Nano Lett.* **24**, 74 (2024).
- [48] X. Z. Yu, N. Kanazawa, W. Z. Zhang, T. Nagai, T. Hara, K. Kimoto, Y. Matsui, Y. Onose, and Y. Tokura, Skyrmion flow near room temperature in an ultralow current density, *Nat. Commun.* **3**, 988 (2012).
- [49] H. Zhang, D. Raftrey, Y.-T. Chan, Y.-T. Shao, R. Chen, X. Chen, X. Huang, J. T. Reichenadter, K. Dong, S. Susarla, L. Caretta, Z. Chen, J. Yao, P. Fischer, J. B. Neaton, W. Wu, D. A. Muller, R. J. Birgeneau, and R. Ramesh, Room-temperature skyrmion lattice in a layered magnet (fe0.5co0.5)5gete2, *Sci. Adv.* **8**, eabm7103 (2022).
- [50] L. Peng, Y. Zhang, L. Ke, T.-H. Kim, Q. Zheng, J. Yan, X.-G. Zhang, Y. Gao, S. Wang, J. Cai, B. Shen, R. J. McQueeney, A. Kaminski, M. J. Kramer, and L. Zhou, Relaxation dynamics of zero-field skyrmions over a wide temperature range, *Nano Lett.* **18**, 7777 (2018).
- [51] Q. Tong, F. Liu, J. Xiao, and W. Yao, Skyrmions in the moiré of van der Waals 2D magnets, *Nano Lett.* **18**, 7194 (2018).
- [52] M. Akram and O. Erten, Skyrmions in twisted van der Waals magnets, *Phys. Rev. B* **103**, L140406 (2021).
- [53] D. Ghader, B. Jabakhanji, and A. Stroppa, Whirling interlayer fields as a source of stable topological order in moiré CrI₃, *Commun. Phys.* **5**, 192 (2022).
- [54] K.-M. Kim, D. H. Kiem, G. Bednik, M. J. Han, and M. J. Park, Ab initio spin hamiltonian and topological noncentrosymmetric magnetism in twisted bilayer CrI₃, *Nano Lett.* **23**, 6088 (2023).
- [55] K.-M. Kim and M. J. Park, Controllable magnetic domains in twisted trilayer magnets, *Phys. Rev. B* **108**, L100401 (2023).
- [56] Q. H. Wang, A. Bedoya-Pinto, M. Blei, A. H. Dismukes, A. Hamo, S. Jenkins, M. Koperski, Y. Liu, Q.-C. Sun, E. J. Telford, H. H. Kim, M. Augustin, U. Vool, J.-X. Yin, L. H. Li, A. Falin, C. R. Dean, F. Casanova, R. F. L. Evans, M. Chshiev, A. Mishchenko, C. Petrovic, R. He, L. Zhao, A. W. Tsen, B. D. Gerardot, M. Brotons-Gisbert, Z. Guguchia, X. Roy, S. Tongay, Z. Wang, M. Z. Hasan, J. Wrachtrup, A. Yacoby, A. Fert, S. Parkin, K. S. Novoselov, P. Dai, L. Balicas, and E. J. G. Santos, The magnetic genome of two-dimensional van der waals materials, *ACS Nano* **16**, 6960 (2022).
- [57] J. Zou, S. K. Kim, and Y. Tserkovnyak, Topological transport of vorticity in heisenberg magnets, *Phys. Rev. B* **99**, 180402 (2019).
- [58] It's noteworthy that these meron textures are carried by the Néel vectors defined in Eq. (4), and their skyrmion numbers should be appropriately interpreted regarding these normalized vectors (see Refs. 84 and 85). We have confirmed that the Néel vectors well characterize the overall magnetic texture excluding the core regions. Further details can be found in the Supplementary Information.
- [59] A. Hubert and R. Schäfer, *Magnetic Domains* (Springer Berlin Heidelberg, 1998).
- [60] T. Song, Q.-C. Sun, E. Anderson, C. Wang, J. Qian, T. Taniguchi, K. Watanabe, M. A. McGuire, R. Stöhr, D. Xiao, T. Cao, J. Wrachtrup, and X. Xu, Direct visualization of magnetic domains and moiré magnetism in twisted 2D magnets, *Science* **374**, 1140 (2021).
- [61] Y. Xu, A. Ray, Y.-T. Shao, S. Jiang, K. Lee, D. Weber, J. E. Goldberger, K. Watanabe, T. Taniguchi, D. A. Muller, K. F. Mak, and J. Shan, Coexisting ferromagnetic-antiferromagnetic state in twisted bilayer

- CrI₃, *Nat. Nanotechnol.* **17**, 143 (2022).
- [62] H. Xie, X. Luo, Z. Ye, Z. Sun, G. Ye, S. H. Sung, H. Ge, S. Yan, Y. Fu, S. Tian, H. Lei, K. Sun, R. Hovden, R. He, and L. Zhao, Evidence of non-collinear spin texture in magnetic moiré superlattices, *Nat. Phys.* **19**, 1150 (2023).
- [63] C. Jiao, S. Pei, S. Wu, Z. Wang, and J. Xia, Tuning and exploiting interlayer coupling in two-dimensional van der waals heterostructures, *Rep. Prog. Phys.* **86**, 114503 (2023).
- [64] F. Xiao, K. Chen, and Q. Tong, Magnetization textures in twisted bilayer CrX₃ (X=Br, I), *Phys. Rev. Research* **3**, 013027 (2021).
- [65] M. Akram, H. LaBollita, D. Dey, J. Kapeghian, O. Erten, and A. S. Botana, Moiré skyrmions and chiral magnetic phases in twisted CrX₃ (X = I, Br, and Cl) bilayers, *Nano Lett.* **21**, 6633 (2021).
- [66] M. Akram, J. Kapeghian, J. Das, R. Valentí, A. S. Botana, and O. Erten, Theory of moiré magnetism in twisted bilayer α -rucl₃, *Nano Lett.* **24**, 890 (2024).
- [67] J. Jena, B. Göbel, T. Ma, V. Kumar, R. Saha, I. Mertig, C. Felser, and S. S. P. Parkin, Elliptical bloch skyrmion chiral twins in an antiskyrmion system, *Nat. Commun.* **11**, 1115 (2020).
- [68] F. Zheng, Magnetic skyrmion lattices in a novel 2D-twisted bilayer magnet, *Adv. Func. Mater.* **33**, 2206923 (2023).
- [69] B. Yang, Y. Li, H. Xiang, H. Lin, and B. Huang, Moiré magnetic exchange interactions in twisted magnets, *Nat. Comput. Sci.* **3**, 314 (2023).
- [70] P. S. Shaban, I. S. Lobanov, V. M. Uzdin, and I. V. Iorsh, Skyrmion dynamics in moiré magnets, *Phys. Rev. B* **108**, 174440 (2023).
- [71] B. Jabakhanji and D. Ghader, Designing layered 2d skyrmion lattices in moiré magnetic heterostructures, *Adv. Mater. Interfaces* **11**, 2300188 (2024).
- [72] N. Sivadas, S. Okamoto, X. Xu, C. J. Fennie, and D. Xiao, Stacking-dependent magnetism in bilayer CrI₃, *Nano Lett.* **18**, 7658 (2018).
- [73] K. W. Song, Interlayer superexchange in bilayer chromium trihalides, *Phys. Rev. B* **107**, 245133 (2023).
- [74] W. Chen, Z. Sun, Z. Wang, L. Gu, X. Xu, S. Wu, and C. Gao, Direct observation of van der Waals stacking-dependent interlayer magnetism, *Science* **366**, 983 (2019).
- [75] M. Gibertini, M. Koperski, A. F. Morpurgo, and K. S. Novoselov, Magnetic 2D materials and heterostructures, *Nat. Nanotechnol.* **14**, 408 (2019).
- [76] J. Kim, K.-W. Kim, B. Kim, C.-J. Kang, D. Shin, S.-H. Lee, B.-C. Min, and N. Park, Exploitable magnetic anisotropy of the two-dimensional magnet cri₃, *Nano Lett.* **20**, 929 (2020).
- [77] L. Webster and J.-A. Yan, Strain-tunable magnetic anisotropy in monolayer crcl₃, crbr₃, and cri₃, *Phys. Rev. B* **98**, 144411 (2018).
- [78] Q.-F. Xu, W.-Q. Xie, Z.-W. Lu, and Y.-J. Zhao, Theoretical study of enhanced ferromagnetism and tunable magnetic anisotropy of monolayer cri₃ by surface adsorption, *Phys. Lett. A* **384**, 126754 (2020).
- [79] C. Tang, L. Zhang, and A. Du, Tunable magnetic anisotropy in 2d magnets via molecular adsorption, *J. Mater. Chem. C* **8**, 14948 (2020).
- [80] M. Tang, J. Huang, F. Qin, K. Zhai, T. Ideue, Z. Li, F. Meng, A. Nie, L. Wu, X. Bi, C. Zhang, L. Zhou, P. Chen, C. Qiu, P. Tang, H. Zhang, X. Wan, L. Wang, Z. Liu, Y. Tian, Y. Iwasa, and H. Yuan, Continuous manipulation of magnetic anisotropy in a van der Waals ferromagnet via electrical gating, *Nat. Electron.* **6**, 28 (2023).
- [81] S. K. Kim and Y. Tserkovnyak, Chiral edge mode in the coupled dynamics of magnetic solitons in a honeycomb lattice, *Phys. Rev. Lett.* **119**, 077204 (2017).
- [82] Z.-X. Li, C. Wang, Y. Cao, and P. Yan, Edge states in a two-dimensional honeycomb lattice of massive magnetic skyrmions, *Phys. Rev. B* **98**, 180407 (2018).
- [83] W. S. Lee, T. Song, and K.-M. Kim, Deep learning methods for hamiltonian parameter estimation and magnetic domain image generation in twisted van der waals magnets, *Mach. Learn.: Sci. Technol.* **5**, 025073 (2024).
- [84] J. Wu, D. Carlton, J. S. Park, Y. Meng, E. Arenholz, A. Doran, A. T. Young, A. Scholl, C. Hwang, H. W. Zhao, J. Bokor, and Z. Q. Qiu, Direct observation of imprinted antiferromagnetic vortex states in coo/fe/ag(001) discs, *Nat. Phys.* **7**, 303 (2011).
- [85] S. Dasgupta, S. K. Kim, and O. Tchernyshyov, Gauge fields and related forces in antiferromagnetic soliton physics, *Phys. Rev. B* **95**, 220407 (2017).